

# A Deep Information Sharing Network for Multi-Contrast Compressed Sensing MRI Reconstruction

Liyan Sun, Zhiwen Fan, Xueyang Fu<sup>✉</sup>, Yue Huang, Xinghao Ding<sup>✉</sup>, and John Paisley

**Abstract**—Compressed sensing (CS) theory can accelerate multi-contrast magnetic resonance imaging (MRI) by sampling fewer measurements within each contrast. However, conventional optimization-based reconstruction models suffer several limitations, including a strict assumption of shared sparse support, time-consuming optimization, and “shallow” models with difficulties in encoding the patterns contained in massive MRI data. In this paper, we propose the first deep learning model for multi-contrast CS-MRI reconstruction. We achieve information sharing through feature sharing units, which significantly reduces the number of model parameters. The feature sharing unit combines with a data fidelity unit to comprise an inference block, which are then cascaded with dense connections, allowing for efficient information transmission across different depths of the network. Experiments on various multi-contrast MRI datasets show that the proposed model outperforms both state-of-the-art single-contrast and multi-contrast MRI methods in accuracy and efficiency. We demonstrate that improved reconstruction quality can bring benefits to subsequent medical image analysis. Furthermore, the robustness of the proposed model to misregistration shows its potential in real MRI applications.

**Index Terms**—Compressed sensing, multi-contrast MRI reconstruction, deep neural networks.

## I. INTRODUCTION

MAGNETIC resonance imaging (MRI) has been widely used to generate anatomically precise images of in-vivo tissue. A major limitation of MRI is the relatively slow data acquisition speed. Compressed sensing (CS) has therefore been used to accelerate MRI by reducing the number of k-space (i.e., Fourier) measurements directly acquired by the machine [1]. CS theory shows how accurate or even perfect

Manuscript received June 1, 2018; revised October 23, 2018; accepted June 13, 2019. Date of publication July 9, 2019; date of current version September 4, 2019. This work was supported in part by the National Natural Science Foundation of China under Grant 61571382, Grant 81671766, Grant 61571005, Grant 81671674, Grant 61671309, and Grant U1605252, in part by the Fundamental Research Funds for the Central Universities under Grant 20720160075 and Grant 20720180059, in part by the CCF-Tencent Open Fund, and in part by the Natural Science Foundation of Fujian Province of China under Grant 2017J01126. The work of L. Sun was supported by Columbia University under China Scholarship Council Grant 201806310090. The associate editor coordinating the review of this manuscript and approving it for publication was Dr. Jan Sijbers. (*Liyan Sun and Zhiwen Fan are co-first authors.*) (*Corresponding author: Xinghao Ding.*)

L. Sun, Z. Fan, Y. Huang, and X. Ding are with the School of Information Science and Engineering, Xiamen University, Xiamen 361005, China (e-mail: dxh@xmu.edu.cn).

X. Fu is with the Department of Automation, University of Science and Technology of China, Hefei 230009, China.

J. Paisley is with the Department of Electrical Engineering, Columbia University, New York, NY 10027 USA.

Digital Object Identifier 10.1109/TIP.2019.2925288

reconstruction can be achieved via appropriate optimizations to fill in the missing Fourier coefficients of k-space [2]. Recently, compressed sensing MRI has been approved by the FDA for GE and Siemens, two major vendors [3]. Hence more MRI scans are expected to be made using compressed sensing methods in clinics, in order to improve patient comfort by speeding up imaging speed. Compressed sensing for magnetic resonance imaging (CS-MRI) is now one of the classic inverse imaging problems in the field of computer vision, but still a very active research topic in medical imaging.

Similar to other image restoration and reconstruction tasks, research on CS-MRI is driven by proposing an effective optimization model for MRI reconstruction. For example, MRI is often modeled with sparsity constraints in a fixed transform bases, e.g., SparseMRI [4], TVCMRI [5], RecPF [6] and FCSA [7], [8]. Limited by the representation ability of such models that use non-adaptive transform bases, other work has been devoted to utilizing the geometric information within images, such as PBDW [9], PANON [10], FDLC [11] and GBRWT [12]. Dictionary learning techniques have also been introduced [13], [14] for adaptive basis learning.

As [12], [13] show, models with adaptive transform bases achieve higher reconstruction quality, but at the expense of heavy computational burden. Furthermore, conventional optimization-based CS-MRI methods are implemented *in situ*, meaning they do not rely on information from MRI training data. The first issue is a clear drawback, while the second may have positive aspects, but the power of deep learning has shown a clear advantage in exploiting big data resources with a deep neural network.

Thus, deep learning has recently been introduced to CS-MRI. For example, Wang *et al.* [15] use a vanilla convolutional neural networks model to learn the mapping from zero-filled MRI to fully-sampled MRI via a massive MRI training set. (Note the term “zero-filled MRI” means the missing Fourier coefficients are replaced by zeros, followed by an inverse 2D FFT.) Sun *et al.* [16] proposed ADMM-NET as a modification of the alternating direction method of multipliers (ADMM) algorithm, where the parameters are inferred via back-propagation. Generative adversarial networks have also been introduced [17], [18]. In other CNN approaches, Lee *et al.* [19] proposed a modified U-shape convolutional neural networks to learn the mapping in the residual domain, while Schlemper *et al.* [20], [21] proposed a *deep cascade convolutional neural network* (DC-CNN) to unroll the standard

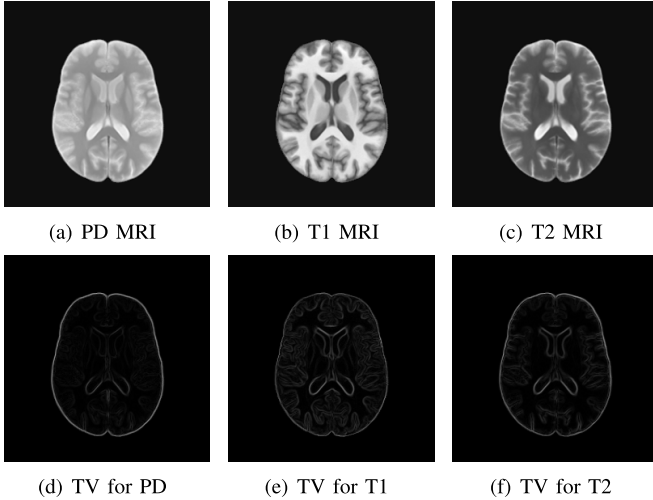


Fig. 1. Multi-contrast MRI images share similar structures.

paradigm of CS-MRI into the deep learning architecture. DC-CNN represents the state-of-the-art performance in *single-contrast* CS-MRI in both imaging quality and speed.

The work mentioned above is based on single-contrast CS-MRI reconstruction. Usually, an MRI scan can obtain images of the same anatomical section under different contrasts, such as T1, T2, and proton-density (PD) weighted MRI generated by applying different MRI protocols [22]. Multi-contrast MRI contains similar, but not the same image structures. By comparing multiple contrast MRI in the same region, radiologists can detect subtle abnormalities such as a developing tumor. This is illustrated in Figure 1(a), 1(b) and 1(c), where PD, T1 and T2 MRI in the SRI24 [23] datasets exhibit similar structures. In the second row of Figure 1 we show the root of sum of squares of the horizontal and vertical gradients of the multi-contrast MR images. Rather than reconstruct each multi-contrast MRI independently, joint reconstruction can provide higher quality images by exploiting such structural similarity.

In this paper, we propose the first deep learning models for multi-contrast CS-MRI reconstruction. We start with two basic networks called *deep independent reconstruction network* (DIRN) and *deep feature sharing network* (DFSN). DIRN uses separate parallel networks to reconstruct each contrast of the MRI where each network is a state-of-the-art DC-CNN architecture [20]. DFSN takes the further step of applying a feature sharing strategy that significantly reduces the number of network parameters. Our final deep learning model, which extends the state-of-the-art results of DFSN, uses a dense connection strategy to transfer information across layers in the network. We call this end-to-end model a *deep information sharing network* (DISN) for multi-contrast CS-MRI inversion. DISN comprises cascaded and densely connected inference blocks consisting of feature sharing units and data fidelity units. In the feature sharing units, all multi-contrast MRI share the same feature maps. We use dense connections to help information sharing at different depths.

Our contributions can be summarized as follows: (1) In the proposed basic DFSN model, the feature sharing unit

fully exploits the similarity among the multi-contrast MRI. The comparative experiments show the DFSN model outperforms DIRN model with multiple amounts of parameters of the independent parallel networks. (2) In the proposed DISN model, the dense connection operation is proposed to propagate the information from lower blocks to deeper blocks directly. The number of parameters only increase linearly rather than quadratically in the regular DenseNet [24]. Even with much fewer network parameters, the dense connection strategy still shows advantages. (3) The experiments on various multi-contrast MRI datasets show the proposed DISN model achieves state-of-the-art performance compared with both single-contrast and multi-contrast MRI methods in imaging quality and speed. The benefit brought by improved reconstruction quality of DISN on posterior medical image analysis is also demonstrated by experiments. (4) The DISN model is robust to the misregistration errors which are common in real MRI acquisition because of large model capacity.

The rest of this paper is organized as follows: Section II summarizes the related work in the field of multi-contrast MRI reconstruction. Section III presents the basic DIRN and DFSN models as well as the proposed DISN model. Section IV compares the different deep learning models and reports the experimental results on various multi-contrast MRI datasets including SRI24 [23], MRBrainS13 [25] and NeoBrainS12 [26]. Section V discusses the network size, testing running time, misregistration environment.

## II. RELATED WORK ON MULTI-CONTRAST CS-MRI

Previous work has exploited the structural correlations in multi-contrast MRI using classic Bayesian and sparse optimization approaches. Suppose we aim at reconstructing  $L$  multi-contrast MRI images, for example  $L = 3$  when PD, T1 and T2 MRI are used. One can formulate this problem as

$$X = \arg \min_X \sum_{i=1}^L \frac{\lambda_i}{2} \|F_{u_i}x_i - y_i\|_2^2 + \rho(X), \quad (1)$$

where  $x_i \in \mathbb{C}^{N \times 1}$  denotes the  $i^{th}$  ( $1 \leq i \leq L$ ) contrast of the complex-valued MR image to be reconstructed and  $X$  indicates the set of all  $x_i$ .  $F_{u_i} \in \mathbb{C}^{M \times N}$  denotes the  $i^{th}$  under-sampled Fourier matrix and  $y_i \in \mathbb{C}^{M \times 1}$  ( $M < N$ ) denotes the  $i^{th}$  k-space measurements. Note that in multi-contrast MRI, it is common to under-sample all the multi-contrast MRI data using different under-sampling masks with the same under-sampling ratio. The first term is the data fidelity unit ensuring consistency between the reconstructed image and measurements.  $\rho(X)$  encodes a regularization term for the MRI contrast images.

Two notable approaches to multi-contrast CS-MRI with which we compare are Bayesian Compressed Sensing by Bilgic *et al.* [27] and FCSA-MT by Huang *et al.* [28]. Bilgic *et al.* base their approach on a modification to Bayesian compressed sensing (BCS) [29] that exploits structural similarity across contrasts. To exploit the structure similarity, the authors cast the problem in the gradient domain, where the prior of the vertical and horizontal gradients of the

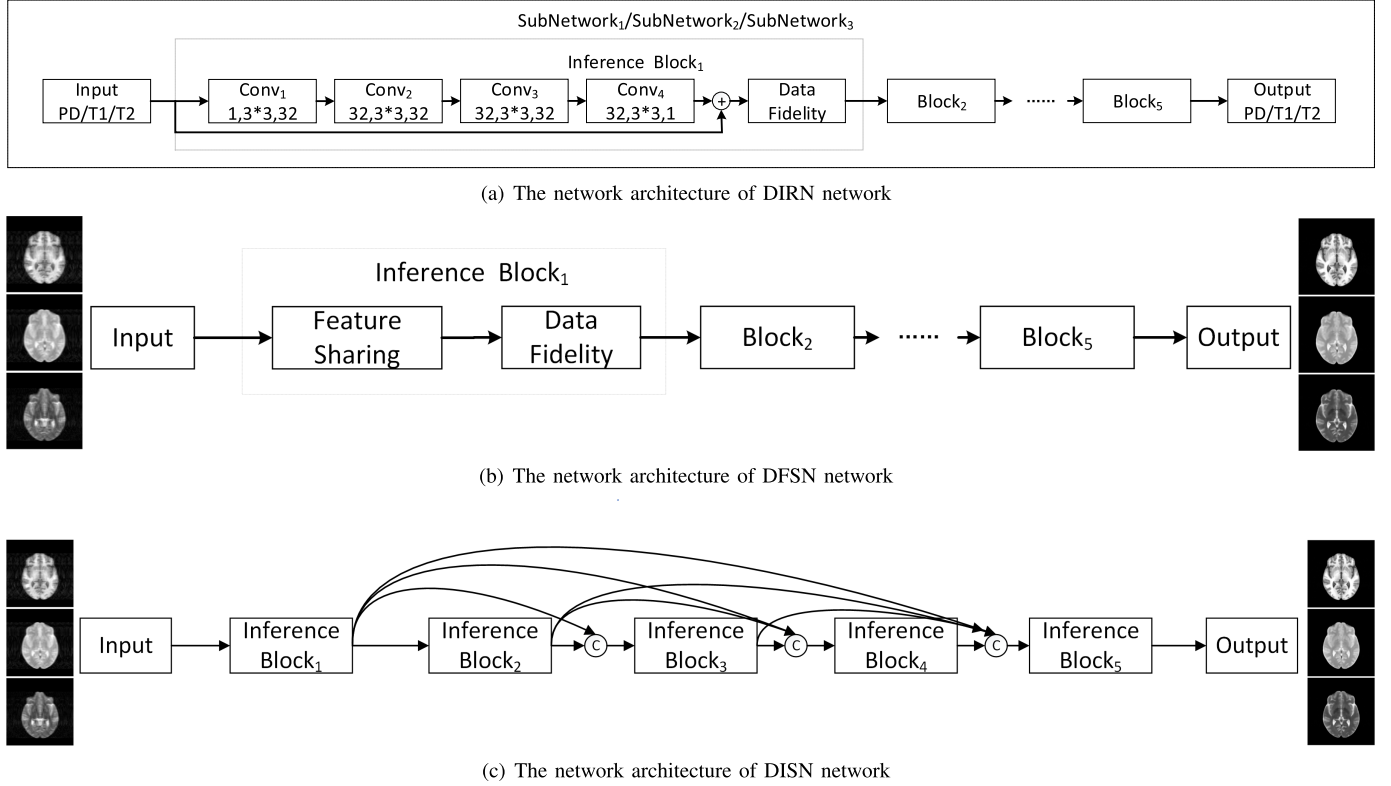


Fig. 2. The network architecture of the proposed DIRN, DFSN, and DISN models for multi-contrast CS-MRI inversion.

multi-contrast MRIs are set to zero-mean Gaussian distributions. A least squared problem can be solved to yield the reconstruction by combining the horizontal and vertical gradients with the k-space data fidelity. The major drawback is running time; requiring about 26 hours to process a set of multi-contrast MRI, the initial algorithm is impracticable in real scenarios, although the authors did later accelerate the model somewhat at the expense of performance [30].

Huang *et al.* extended the FCSA [7], [8] algorithm from single-contrast to multi-contrast MRI (FCSA-MT) [28], [31]. The FCSA-MT model is based on the observations that the variance of the gradients should be similar in the same spatial positions across MRI, and wavelet coefficients should have similar non-zero support in the same anatomical sections. The FCSA-MT model achieves this through a linear model based on squared error, group sparsity and total variation minimization. Misregistration settings can also lead to drastic performance reduction since the group sparsity is no longer accurately aligned. Li *et al.* later accelerated FCSA-MT using fast conditioning [32].

### III. A DEEP INFORMATION SHARING NETWORK (DISN)

We propose a deep learning model that takes a set of sub-sampled Fourier k-space measurements at multiple contrasts,  $y_1, \dots, y_L$ , and outputs the corresponding reconstructed images at each contrast  $x_1, \dots, x_L$ . The model learns how to exploit structural similarities across contrasts to produce an output that is significantly better than could be obtained via  $L$  independent inversion algorithms. Because this represents the

first deep learning approach to the problem, we experiment with three different deep structures, but the best-performing structure is a “deep information sharing network” (DISN). This network consists of cascaded blocks with dense connections. Within each block, we adopt a feature sharing unit combined with a data fidelity unit. Below, we describe the feature sharing and data fidelity units, and how they are combined to form the inference block. We then discuss how the blocks are densely connected.

#### A. Feature Sharing Unit

An intuitive approach to multi-contrast CS-MRI inversion is to simply reconstruct them separately with a deep learning model, for example as shown in Figure 2(a). We call this a *deep independent reconstruction network* (DIRN). The DIRN model shown is made up of several parallel subnetworks. Here we plot 3 subnetworks for PD, T1 and T2 contrasts. The architecture of each subnetwork is the state-of-art DC-CNN architecture [20]. If each subnetwork consists of  $N$  inference blocks, we call it DIRN- $N$ B. (All the subnetworks share the same number of blocks.) Here we adopt 5 blocks, DIRN-5B. Each building block consists of 4 convolutional layers with global shortcut and a data fidelity unit (we will discuss this later) as shown in Figure 2(a). The global shortcut uses a skip connection architecture in the feature sharing unit within a block to help stabilize the training [20]. In each block, the first convolutional layer is used to map the MRI to multiple feature maps and the last convolutional layer integrates the feature maps into a single reconstruction in the residual domain.

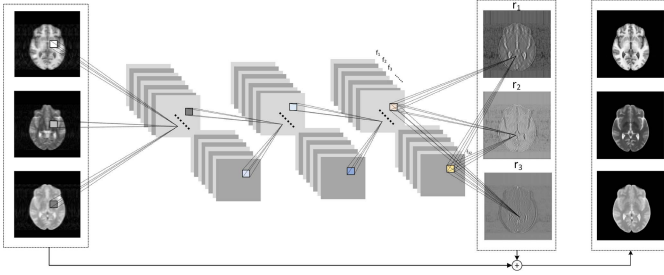


Fig. 3. The feature sharing unit.

Leaky ReLU is used as an activation function, except for the last convolutional layer where the identity mapping is used. There are no interactions among these subnetworks. In such a deep learning network setting, large amounts of MRI data is used to learn the complex patterns of each multi-contrast MRI separately.

Although DIRN may provide a powerful modeling ability for each contrast of the MRI, the number of network parameters triples because there are three subnetworks. As showed in Figure 1, structural similarity should be exploited in deep neural network architectures, both to achieve better reconstruction and also with the aim of reducing parameters. Hence we also consider a *deep feature sharing network* (DFSN) as shown in Figure 2(b). Similar to DIRN, the DFSN consists of 5 cascaded inference blocks, DFSN-5B, while each block is made up of a feature sharing unit and a data fidelity unit. Multi-contrast MRI such as T1, T2 and PD zero-filled MR magnitude images are input to the DFSN in a stack as the multi-channel input. The DFSN network can therefore reconstruct multi-contrast MRI data simultaneously. We show the feature sharing unit in Figure 3. In traditional multi-contrast MRI methods, the structural similarity is modeled in the finite difference domain; instead we adopt *residual learning* in the feature sharing unit. Similarly, each feature sharing unit contains 4 convolutional layers with the same number of filters as the single subnetwork of DIRN in each layer and all activation functions are Leaky ReLU, except for the identity mapping in the last layer.

**1) Discussion:** The proposed feature sharing strategy has a similar motivation to traditional sparse representation methods. In each feature sharing unit, we denote the residuals for the  $j^{th}$  ( $1 \leq j \leq L$ ) contrast MRI as  $r_j$ . As mentioned, for the last convolutional layer in the unit, the activation function is set to the identity function, thus  $r_j = \sum_i f_i w_{ij}$ , where the  $f_i$  denotes the  $i^{th}$  feature map for the last convolutional layer in the unit, and  $w_{ij}$  denotes the corresponding kernel in Toeplitz matrix form. In the classic dictionary learning formulation, the signal can be approximated as  $s = D\alpha$ , or equivalently  $s = \sum_i d_i \alpha_i$ .  $d_i$  is the  $i^{th}$  column of the dictionary  $D$  and  $\alpha_i$  is the  $i^{th}$  entry of the sparse coefficients  $\alpha$ .

In previous work such as the ScSR model for image super-resolution [33], [34], the patches of high and low resolution images share the same sparse coefficients  $\alpha_j$  yet different dictionaries  $D_h$  and  $D_l$ . In such setting, the correlation between low and high resolution image patches may be overlooked. In the DFSN model, something similar to

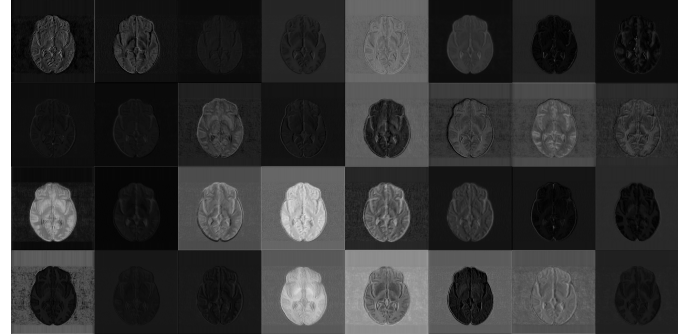


Fig. 4. The feature maps from the last convolutional layer in the feature sharing unit within the last block of the DFSN-5B model.

high-resolution and low-resolution dictionaries are inferred simultaneously in the form of  $f_i$  with the representation coefficients  $w_{ij}$  via a large dataset. In Figure 4, we show the feature maps  $f_i$  ( $1 \leq i \leq 32$ ) for the last convolutional layer in the feature sharing unit of the 5th block with the DFSN-5 model. We observe that they contain enough diversity to represent the structures in PD, T1 and T2 MRI, thus validating the feature sharing strategy.

### B. Data Fidelity Unit

We also use the data fidelity unit from [20] within each block to reduce bias by enforcing more accurate values on the sampled positions in k-space. Following Equation 1, we solve the following objective function in the data fidelity unit for each contrast,

$$x_i = \arg \min_{x_i} \frac{\lambda_i}{2} \|F_{u_i} x_i - y_i\|_2^2 + \frac{1}{2} \|x_i - x_{in_i}\|_2^2, \quad (2)$$

where  $x_{in_i}$  is the input to the data fidelity unit and  $\lambda_i$  is the regularization parameter. To enforce consistency between the reconstruction and the measurements  $y_i$ , we set  $\lambda_i$  to a large value, e.g.,  $10^6$ , which only penalizes deviation from these measured locations. The second term can be viewed as the prior guess, where the input image  $x_{in_i}$  is the output by the feature sharing unit. We observe that these fidelity units are calculated independently for each contrast, but each input  $x_{in_i}$  is constructed by sharing information across contrasts in the deep learning model.

We can simplify by working in the Fourier domain, after which the solution using element-wise division is

$$x_i = F^H \frac{\lambda F F_{u_i}^H y_i + F x_{in_i}}{\lambda F F_{u_i}^H F_{u_i} F^H + I}, \quad (3)$$

where the term  $F F_{u_i}^H y_i$  is the Fourier transform of the zero-filled reconstruction, the term  $F F_{u_i}^H F_{u_i} F^H$  is a diagonal matrix with ones at the sampled locations and zeros otherwise. Calling the feed forward function for this unit  $g(x_{in_i}; y_i; \lambda)$ , the relevant gradient for model training is

$$\frac{\partial g}{\partial x_{in_i}^T} = \frac{I}{\lambda F F_{u_i}^H F_{u_i} F^H + I}. \quad (4)$$

We will also study the impact of using different norm regularization on the network performance in future work [35].

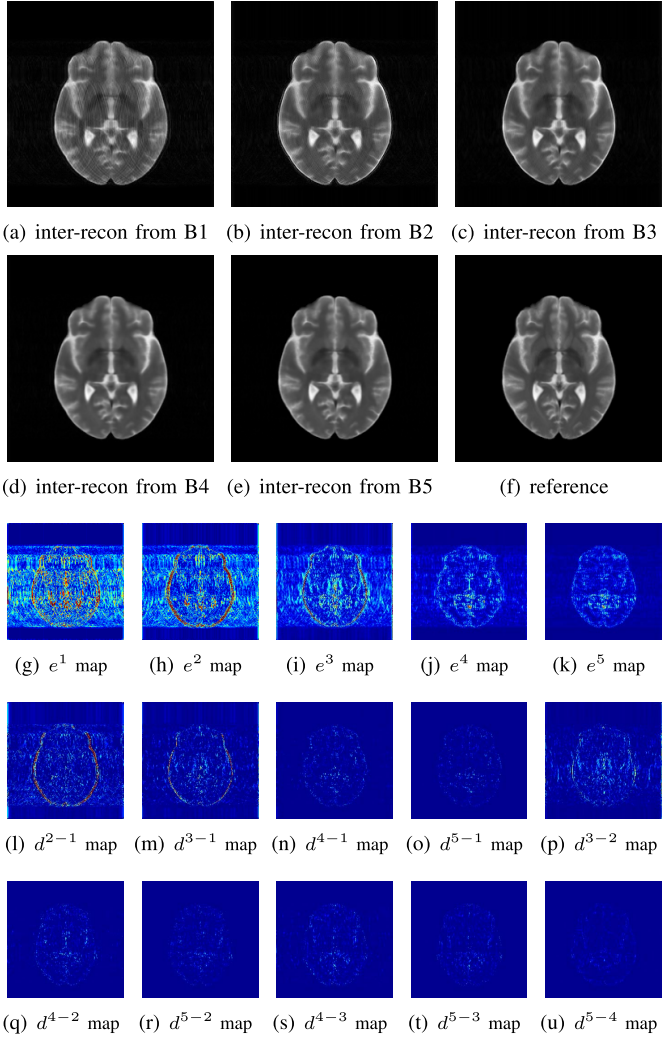


Fig. 5. The intermediate reconstructions and their error maps from each block, as well as the error differential maps.

### C. Dense Connections

We proposed DFSN to share information across contrasts of the MRI. We visualize the intermediate reconstructions of T2 brain MRI by the inference blocks of DFSN-5B model in Figure 5. The test data is under-sampled with 1D 20% Cartesian mask given in Figure 7. We observe that the outputs of the inference blocks improve as the network becomes deeper. To further analyze the reconstruction quality of each block, we conduct the following experiments:

We define the pixel-wise absolute reconstruction error map as  $e^i = |x^i - x^{fs}|$  where  $x^i$  represents the output produced by the  $i$ th block and  $x^{fs}$  the full-sampled ground truth MRI. We plot the  $e^i$  maps of the T2 intermediate reconstruction of the DFSN-5B model from the first to the fifth block in the third row of Figure 5. In the fourth and fifth rows, we show positive error map differences of shallow  $n$ th blocks with deep  $m$ th blocks defined as  $d^{m-n} = (e^m - e^n)_+$  ( $n < m$ ) where the  $(\cdot)_+$  represents only retaining the nonnegative values, meaning we focus on the positions where the lower block achieves high reconstruction accuracy. As the blocks get deeper, we observe that the intermediate reconstructions from lower blocks show

less advantages. We conclude that intermediate reconstructions from lower blocks contain valuable information lost to deeper levels.

These observations can also be interpreted from the viewpoint of “information bottleneck” theory [36]–[38]. In this theory, deep neural networks process the information flow by “squeezeing” it out through a bottleneck to remove the irrelevant noisy details and only retain the features most relevant for high-level abstraction. In our case, noisier artifacts due to under-sampling are reduced with deeper cascaded blocks. However, as a side effect the structural details are at risk of being eliminated.

Motivated by this analysis, we densely connect the inference blocks in DFSN and propose a *deep information sharing network* (DISN). In Figure 2(c), we show the network architecture of the DISN-5B model. Information sharing is performed in two ways: (1) the information between the multi-contrast MRI is shared via the feature sharing unit, and (2) the information in the deeper inference blocks is shared by dense connections using concatenations. Each block in DISN receives the output from all previous blocks as its input. In the recent work called Semi Parallel Deep Neural Network (SPDNN) model [39], a parallel network with different architectures is used and merged into a single network. With the SPDNN idea applied on every block in the DFSN model, the resulting network architecture leads to our proposed DISN model.

As with DenseNet [24], where the feature maps are densely fed to deeper layers by concatenation, the dimension of the channels in deeper layers may explode quadratically, limiting the depth of the model. Motivated by DenseNet and the similar MemNet [40], DISN is different in that only the intermediate reconstructed MRI images are concatenated rather than the large number of feature maps. As a consequence, the dimensionality only increases linearly in the channel according to the number of contrasts.

## IV. EXPERIMENTS

### A. Datasets

We conduct experiments on three multi-contrast MRI datasets: the SRI24 atlas [23], MRBrainS13 benchmark [25] and NeoBrainS12 benchmark [26]. We train separate networks of the training data of each dataset and test on their respective testing data.

**1) SRI24 Atlas:** The multi-contrast brain MRI data was obtained on a 3.0T GE scanner with 8-channel head coil with three different contrast setting: For T1-weighted MRI data: 3D axial IR-prep SPoiled Gradient Recalled (SPGR), TR = 6.5ms, TE = 1.54ms, number of slices = 124, slice thickness = 1.25mm. For T2-weighted (late echo) and PD-weighted (early echo) MRI data: 2D axial dual-echo fast spin echo (FSE), TR = 10s, TE = 14/98ms, number of slices = 62, slice thickness = 2.5mm. The field-of-view covers a region of 240 × 240mm with resolution 256 × 256 pixels. The SRI24 dataset contains 407 T1w-T2w-PD MRI training pairs. We randomly select 36 multi-contrast MRI data pairs as test data, while the others are used for training.

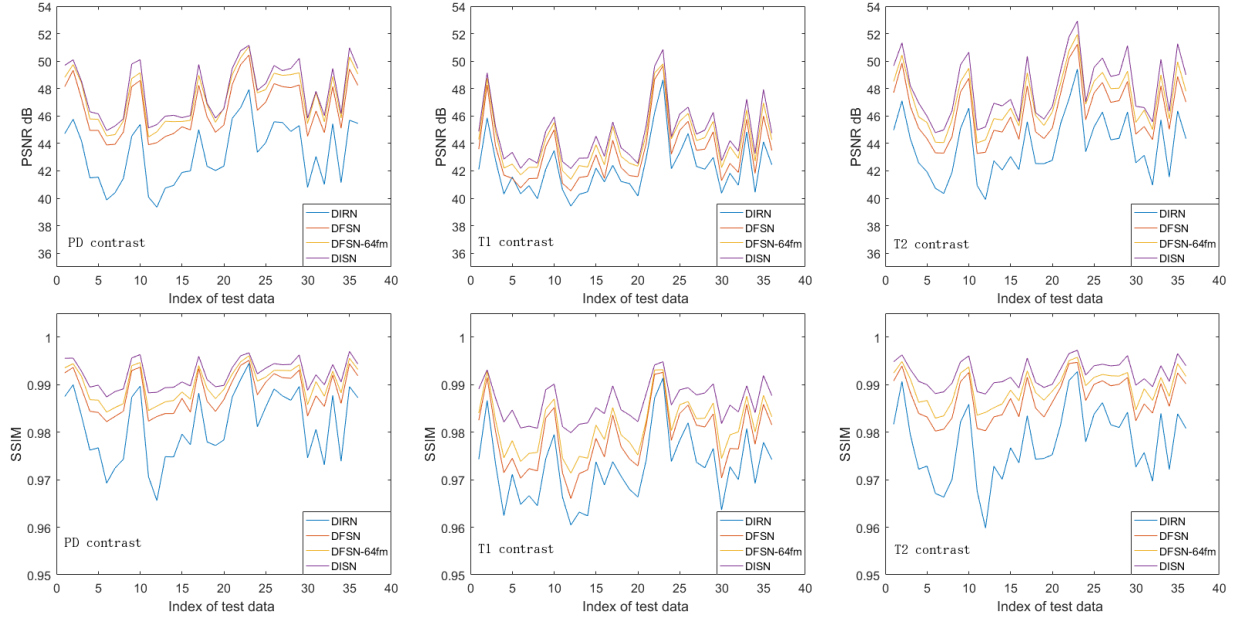


Fig. 6. The performance of DIRN-5B, DFSN-5B, DFSN-5B with 64 feature maps and DISN-5B on all 36 test MRI in SRI24 datasets (x-axis).

2) *MRBrainS*: Twenty fully annotated multi-contrast (T1-weighted, T1-weighted inversion recovery and T2-FLAIR) 3T MRI brain scans with the size  $240 \times 240$  are provided in the Grand Challenge on MR Brain Image Segmentation (MRBrainS) workshop at MICCAI2013. The voxel size of T1, T1-IR and T2-FLAIR MRI is  $0.958\text{mm} \times 0.958\text{mm} \times 3.0\text{mm}$ ,  $0.958\text{mm} \times 0.958\text{mm} \times 3.0\text{mm}$  and  $0.958\text{mm} \times 0.958\text{mm} \times 3.0\text{mm}$  respectively. These scans have been acquired at the University Medical Center Utrecht from patients with diabetes and matched controls with increased cardiovascular risk with varying degrees of atrophy and white matter lesions (age  $> 50$ ). These abnormalities have different appearances in different contrasts. The 20 scans contains 320 pairs of multi-contrast MRI data in total, we randomly select 80% of the slices for training and the others for testing.

3) *NeoBrainS*: Unlike MRBrainS, which is acquired on the adult, the grand challenge in MICCAI2012 called Neonatal Brain Segmentation (NeoBrainS) provides the multi-contrast (T1-weighted and T2-weighted) MRI scans of neonatal brains. All 7 scans containing 175 multi-contrast MRI data pairs of size  $512 \times 512$  are acquired using a Philips 3T system at the University Medical Center Utrecht. The detailed imaging parameters can be found in [26]. We also randomly select 80% of the slices as training datasets and 20% as testing datasets.

4) *Loss Function*: The loss function for DIRN, DFSN and DISN is

$$L(x_i^{zf}, x_i^{fs}) = \frac{1}{3} \sum_{i=1}^L \|x_i^{fs} - f_i(x_i^{zf}; \theta_i)\|_2^2 \quad (5)$$

where  $x_i^{zf}$  and  $x_i^{fs}$  are zero-filled and fully-sampled magnitude MRI, respectively, for the  $i$ th contrast. The  $\theta_i$  represents the network parameters for each subnetwork for DIRN, while in DFSN and DISN, they are incorporated in the single feature sharing unit.

5) *Implementation*: For training, we learn our models using TensorFlow for the Python environment on an NVIDIA Geforce GTX 1080Ti board with 11GB GPU memory and Intel Xeon CPU E5-2683 at 2.00GHz. For each block of the feature sharing unit, we use 4 convolutional layers followed by Leaky ReLU activation functions with 0.2 negative slope. For each convolutional layer, we obtain 32 shared feature maps except for the first and last convolutional layer, where 3 feature maps are used for the contrast residuals. These settings are applied to both DFSN and DISN. For the DIRN model, the first and last convolutional layer in the inference block has only one feature map since the 3 contrasts are reconstructed using 3 different deep learning networks. The kernel size is set to  $3 \times 3$  and padding is used to keep the size of feature maps unchanged. We apply Xavier initialization for all models and train for 40000 iterations using ADAM. We select the initial learning rate to be 0.0005, the first-order momentum to be 0.9 and the second momentum to be 0.999. Each mini-batch contains 4 whole MRI data pairs. We use whole MRI instead of cropped patches as input since the data fidelity unit requires the entire under-sampled k-space data. We do not use batch normalization in our model.

### B. Training and parameter details

1) *Data Augmentation*: We use data augmentation on the entire training set of SRI24 Atlas datasets and MRBrainS13 benchmark to avoid overfitting. We use horizontal and vertical flips on each training data, thus tripling the total number of training data.

### C. Deep Learning Model Comparison

We compare DIRN, DFSN and DISN on the SRI24 atlas datasets to check the utility of feature sharing and dense connection strategies. In Figure 6, we show the network

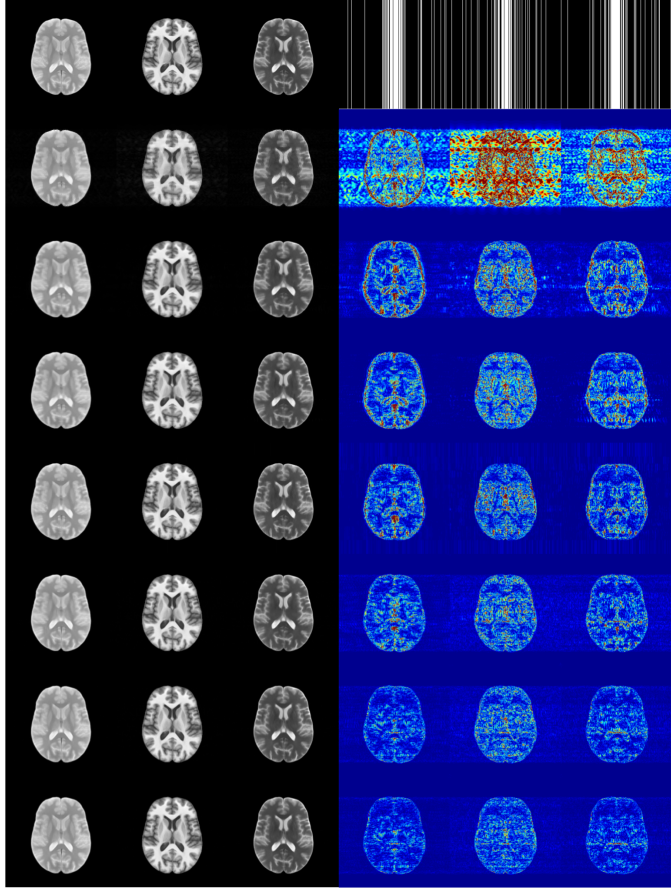
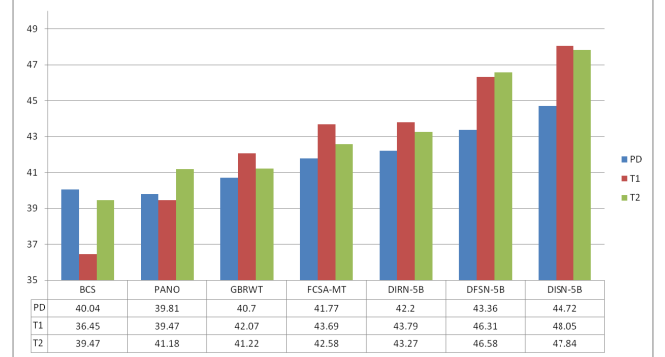


Fig. 7. The reconstruction results: the first row is the fully-sampled MRI with different 1D Cartesian 20% masks. From the second to eighth rows we show BCS, PANO, GBRWT, FCSA-MT, DIRN-5B, DFSN-5B and DISN-5B on a testing multi-contrast MRI data in SRI24 datasets. From left to right, each row contains the PD, T1 and T2 reconstructions and error images. The display of the error maps range from 0 to 0.1.

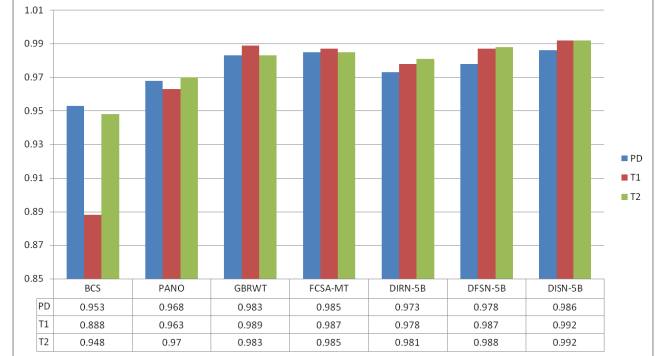
performance of DIRN-5B, DFSN-5B and DISN-5B on test data (indexing has been permuted). We use the under-sampling pattern in Figure 7. Compared with DIRN, DFSN shows the benefit of feature sharing, while DISN has further improvement by exploiting information across depths through dense connections. The number of parameters of DFSN-5B is  $101K$ , far fewer than DIRN-5B ( $286K$ ), while DISN-5B also has slightly more parameters ( $106K$ ) because of extra kernels used in the dense connections. We also ran the experiment with 64 feature maps for DFSN-5B, resulting in  $387K$  parameters and found that DISN-5B still achieves higher reconstruction quality with 32 feature maps. In Figure 6 we show all results for 32 maps and one result for 64 maps.

#### D. Model Comparisons on the SRI24 Datasets

On the SRI24 dataset, we compare the proposed DISN-5B model and its more basic versions DIRN-5B and DFSN-5B model with single-contrast MRI methods PANO [10], GBRWT [12] and state-of-the-art multi-contrast methods, such as BCS [27] and FCSA-MT [31], using three different 1D Cartesian masks with the same sampling ratio of 20%. The parameter setting of the non-deep optimization models has been tuned to their best values. The reconstructions and error residual images



(a) PSNR



(b) SSIM

Fig. 8. The PSNR and SSIM of single- and multi-contrast CS-MRI inversion algorithms averaged over the 36 test images under different 1D Cartesian 20% masks. Deep learning models clearly outperform in PSNR due to their L2 minimization objective function. The structural similarity (SSIM) measure is more competitive.

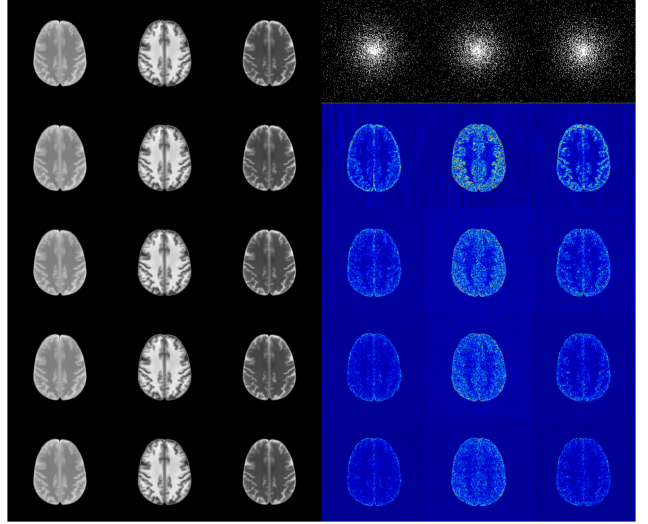


Fig. 9. Reconstruction results for comparison: the first row is the fully-sampled MRI with different 2D random 10% masks. From the second row to fifth row, we show FCSA-MT, DIRN-5B, DFSN-5B and DISN-5B on a multi-contrast MRI test data from the SRI24 dataset. From left to right are the PD, T1 and T2 reconstructions respectively. The display of the error maps range from 0 to 0.1.

are shown in Figure 7. We see that the visual quality of DISN outperforms other methods, providing better preservation for structural details. This is supported by objective quantitative

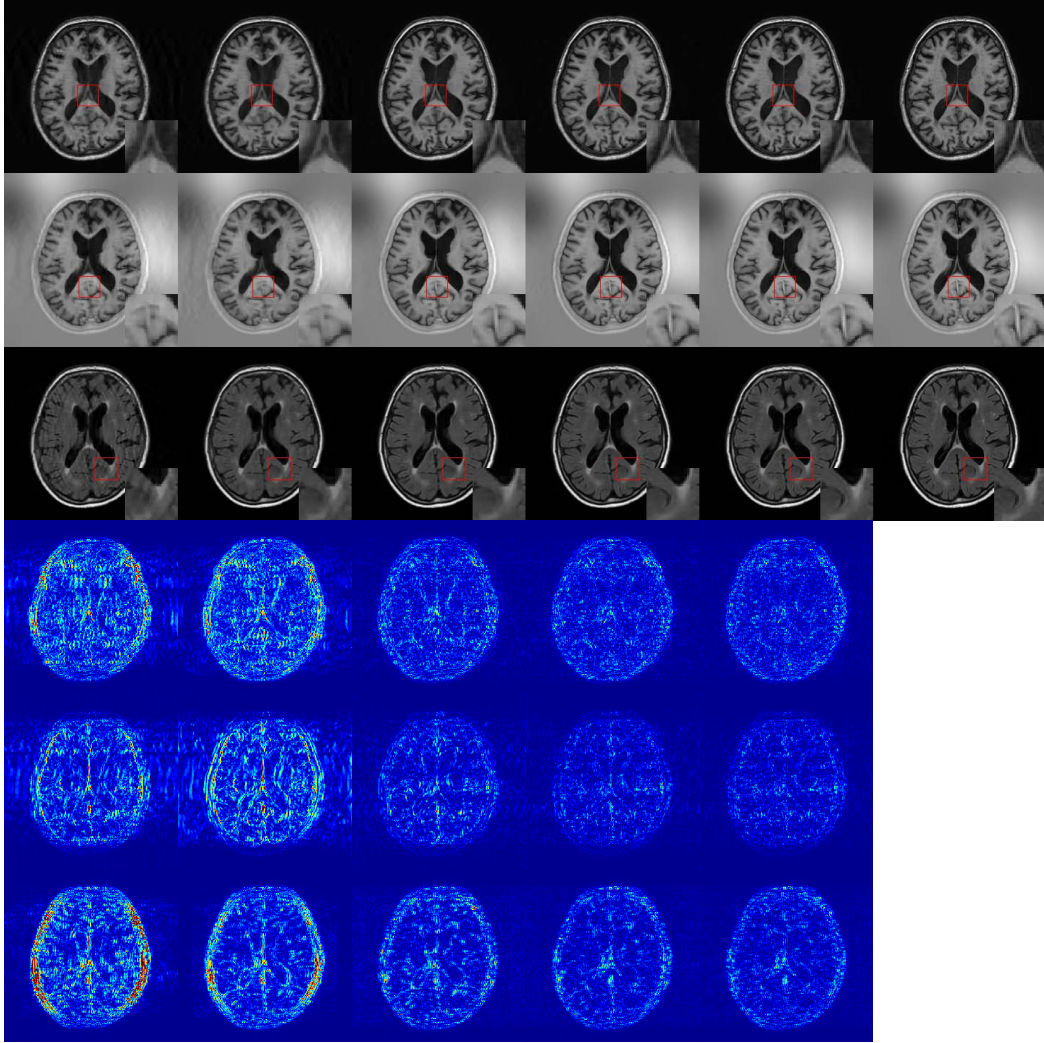


Fig. 10. In the first row (T1 contrast), second row (T1-IR contrast), and third row (T2-FLAIR contrast), we show the MR images of FCSA-MT, GBRWT, DIRN-5B, DFSN-5B, DISN-5B and fully-sampled from left to right on a multi-contrast MRI test data from the MRBrainS benchmark. In the last three rows, we show the corresponding reconstruction error maps. The error display ranges from 0 to 0.15.

measures of PSNR and SSIM, which we show in Figures 8(a) and 8(b). We find that a plain deep learning model like DIRN and DFSN already achieves good performance on the task, while the proposed DISN model achieves the best performance. We further test DISN using three different 2D random masks with sampling ratio of 10%, and compare with FCSA-MT, DIRN and DFSN. These reconstruction results are shown in Figure 9. The experiment supports that DISN generalizes well to 2D random sampling pattern with lower under-sampling ratios.

#### E. Model Comparisons on the MRBrainS Datasets

The standard scans in the SRI atlas contain no lesions of the brain. Therefore, we also test our proposed model on the multi-contrast MRI dataset MRBrainS, where the scans were acquired on patients with varying degree of white matter lesions (WML). We use 3 different 1D 20% Cartesian masks for under-sampling, as shown in Figure 7.

In Table I we observe that the proposed DISN-5B still outperforms the comparison algorithms, followed by DFSN-5B.

We show the reconstructions on a representative multi-contrast test MRI in Figure 10. From these experiments, we observe that DISN model still works well in more complicated and diverse multi-contrast MRI settings. The deep neural network we use is flexible enough to model the structural similarities while still distinguishing differences across multi-contrast MRI, especially within the abnormalities. For example, the white matter lesions regions are better recovered using the proposed DISN model, as shown in Table I, providing more reliable diagnostic information. In Figure 11, we plot the averaged PSNR and SSIM curves on the test data from the MRBrainS benchmark with different under-sampling ratios. These experiments results give evidence that the proposed DISN is robust to different under-sampling ratios.

The MRI data of MRBrainS are hand-annotated with segmentation labels. We thus can test the MRI reconstructed by various CS-MRI models as inputs to the state-of-the-art medical image segmentation model called U-Net [41] (with pixel-wise cross-entropy as loss function). The U-Net model is trained on fully-sampled MRI and label pairs. We adopt

TABLE I  
AVERAGE PSNR | SSIM OF CS-MRI METHODS ON TEST DATA. WE ALSO GIVE THE EVALUATION INDEX FOR THE REGIONS OF WML

| Regions | Whole Brain          |                      |                      | Regions of WML       |                      |                      |
|---------|----------------------|----------------------|----------------------|----------------------|----------------------|----------------------|
|         | T1                   | T1-IR                | T2-FL                | T1                   | T1-IR                | T2-FL                |
| BCS     | 28.77   0.854        | 30.92   0.922        | 29.40   0.788        | 27.80   0.816        | 28.27   0.852        | 29.39   0.851        |
| PANO    | 32.82   0.928        | 32.81   0.953        | 33.48   0.926        | 30.83   0.893        | 29.77   0.901        | 31.89   0.902        |
| GBRWT   | 33.16   0.939        | 33.10   0.958        | 33.91   0.943        | 31.00   0.896        | 30.17   0.909        | 32.07   0.901        |
| FCSA-MT | 32.59   0.934        | 34.73   0.967        | 31.57   0.915        | 31.12   0.899        | 32.22   0.928        | 31.53   0.892        |
| DIRN-5B | 36.48   0.967        | 37.54   0.978        | 34.52   0.935        | 33.87   0.935        | 33.70   0.944        | 32.90   0.916        |
| DFSN-5B | 37.17   0.969        | 39.80   0.984        | 35.71   0.949        | 34.77   0.942        | 36.41   0.963        | 34.22   0.937        |
| DISN-5B | <b>37.65   0.972</b> | <b>40.54   0.985</b> | <b>36.53   0.955</b> | <b>35.01   0.943</b> | <b>37.07   0.966</b> | <b>35.27   0.942</b> |

TABLE II

DICE COEFFICIENTS USING THE U-NET SEGMENTATION NETWORK ON THE RECONSTRUCTED T2-CONTRAST MRI. THE SEGMENTED TISSUES INCLUDE GRAY MATTER (GM), WHITE MATTER (WM) AND CEREBROSPINAL FLUID (CSF). DISN-5B BEST APPROXIMATES THE FULLY-SAMPLED IMAGE

| DC % | FCSA-MT | GBRWT | DIRN-5B | DFSN-5B | DISN-5B      | Fully-Sampled |
|------|---------|-------|---------|---------|--------------|---------------|
| GM   | 66.53   | 70.09 | 70.58   | 75.88   | <b>76.41</b> | 77.93         |
| WM   | 77.66   | 79.30 | 79.90   | 84.56   | <b>85.03</b> | 85.84         |
| CSF  | 73.85   | 75.81 | 77.96   | 80.53   | <b>80.97</b> | 81.68         |

the widely-used Dice Coefficients (DC) as the quantitative measure to evaluate segmentation quality. These DC results are shown in Table II averaged over the test data (DC index is given in percentage with higher score means better segmentation). Also, we show the segmentation comparisons in Figure 12. We observe that the better reconstruction of DISN leads to a more accurate segmentation, which is near the upper bound performance of the segmentation produced by U-Net on the fully-sampled MRI. The proposed multi-contrast DISN model can thus have significant benefits in downstream medical image analysis tasks.

#### F. Model Comparisons on the NeoBrainS Datasets

In addition to the multi-contrast MRBrainS benchmark data acquired from patients over 50 years old, we also test on the neonatal brain MRI in the NeoBrainS benchmark. Neonatal brains grow rapidly and develop a wide range of cognitive and motor functions, which are critical factors in many neurodevelopmental and neuropsychiatric disorders, such as schizophrenia and autism. DIRN-5B, DFSN-5B and DISN-5B are trained and tested on the training datasets in NeoBrainS benchmark with a 10% Cartesian under-sampling mask of the size  $512 \times 512$ . We show the reconstructed MRI images of DIRN-5B, DFSN-5B and DISN-BB and their corresponding error maps in Figure 13. We observe that DISN-5B again achieves the optimal reconstruction quality. In Figure 14, we give the averaged PSNR and SSIM evaluation of the three compared deep learning models, which is consistent with the visual assessments.

## V. DISCUSSION

The experimental results on three different multi-contrast MRI datasets support that the proposed DISN model generalizes well to healthy adult brain MRI, brain MRI datasets with

pathological abnormalities and neonatal brain MRI, all under different under-sampling patterns and under-sampling ratios. In this section, we provide additional performance details and analysis of our model.

#### A. Converge Analysis

In Figure 15 we show the training loss curve on the SRI24 atlas dataset as a function of iteration using the mask from Figure 7. We observe that the convergence for these deep learning models is relatively fast, and DISN gives a network with best training loss.

#### B. Network Size

We also show DISN model performance by adjusting the number of cascaded blocks from 1 to 11 and give these results in Figure 16 for the SRI24 dataset using 1D Cartesian 20% under-sampling. We find that as the number of blocks increases, the network performance steadily increase with smaller marginal improvement before finally reach convergence, while the DISN-5B model already achieves state-of-the-art performance in multi-contrast CS-MRI reconstruction.

#### C. Testing Running Time

In Table III we compare the running times for different models on test time data using the SRI24 dataset. For the optimization-based single- and multi-contrast MRI methods, additional optimizations are required on test images, making processing of a new MRI more time-consuming. On the other hand, for DIRN-5B, DFSN-5B and DISN-5B, the reconstruction is much faster because the model is feed-forward and no iterations are required.

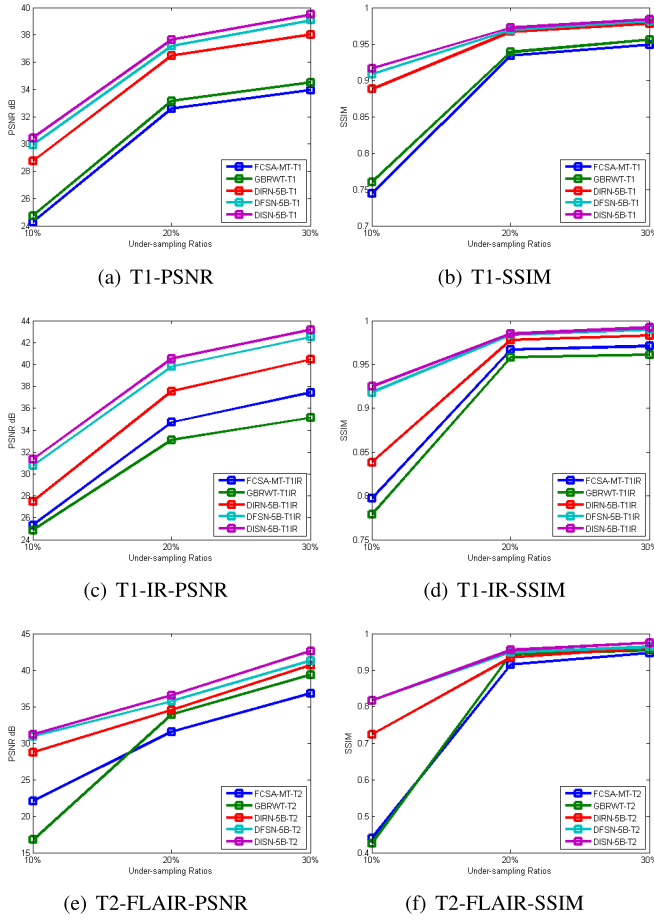


Fig. 11. The averaged PSNR and SSIM comparisons of the FCSA-MT, GBRWT, DIRN-5B, DFSN-5B and DISN-5B reconstruction on 10%, 20% and 30% 1D Cartesian under-sampling patterns. All the three contrast MRI (T1, T1-IR and T2-FLAIR) are shown. The proposed DISN model achieves the best performance.

TABLE III  
TEST RUNTIME COMPARISON (DEEP MODELS USE 5 BLOCKS)

| BCS   | PANO  | GBRWT | FCSA-MT | DIRN  | DFSN  | DISN  |
|-------|-------|-------|---------|-------|-------|-------|
| 30min | 19.6s | 64.6s | 5.7s    | 0.17s | 0.11s | 0.18s |

#### D. Misregistration Environment

The multi-contrast MRI datasets used in this paper have already undergone registration, i.e., been made to overlap as well as possible. However, in real MRI scenarios, assuming such accurate registration is not always realistic. For traditional optimization-based multi-contrast MRI methods such as FCSA-MT, this registration must be strictly enforced because of the rigid sparsity assumption in these models. However, for the proposed DISN the trained network is quite robust to the shifts that are normal in the real-world MRI scanning process.

In this experiment, we take the SRI24 datasets as an example and train the DISN-5B model with randomly shifted MRI data pairs in the small range within 2 pixels in all directions. We then test the DISN model on the position-fixed PD, T1 and position-shifted T2 data in the test datasets. The T2 data is also shifted by up to 2 pixels in all directions.

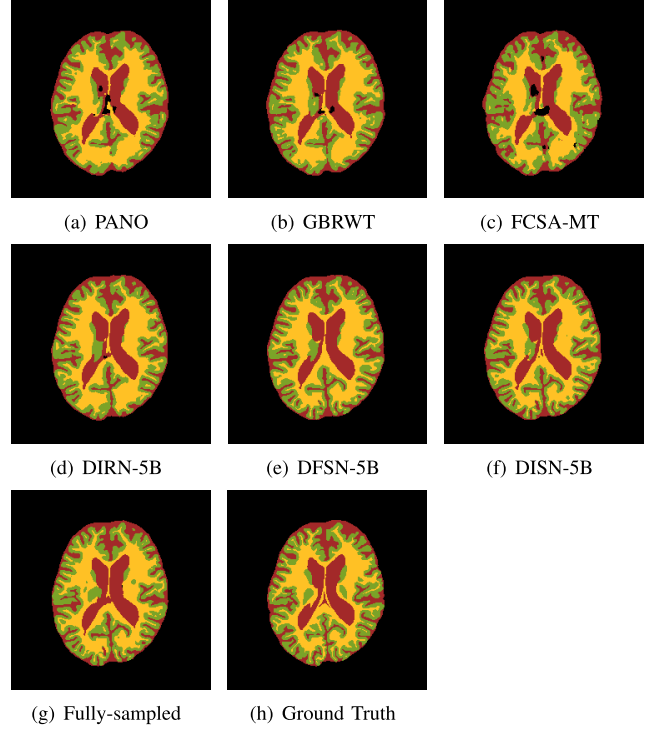


Fig. 12. Post-reconstruction segmentation results produced by state-of-the-art U-Net segmentation model. Segmentation performed on outputs from single-contrast CS-MRI methods (PANO, GBRWT) and multi-contrast CS-MRI methods (DIRN-5B, DFSN-5B and DISN-5B).

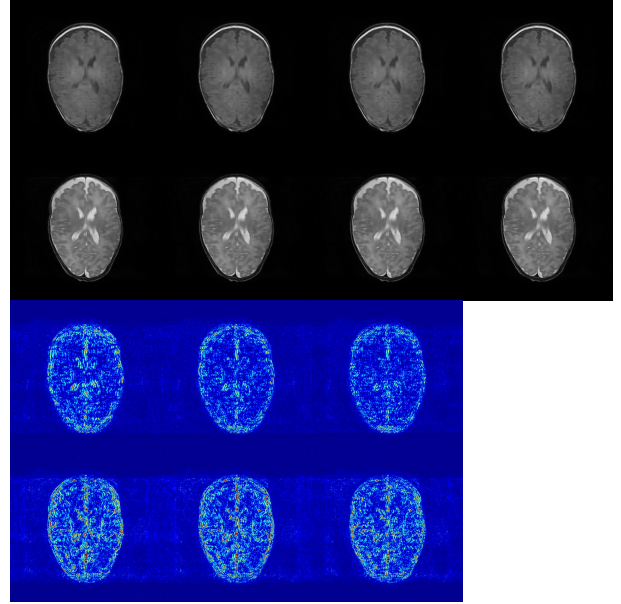


Fig. 13. In the first row (T1 contrast), second row (T2 contrast), we show the MR images of DIRN-5B, DFSN-5B, DISN-5B and full-sampled from left to right on a testing multi-contrast MRI data in NeoBrain benchmark. In the last three rows, we show the corresponding reconstruction error maps. The error display ranges from 0 to 0.1.

(We use the under-sampling masks shown in Figure 7.) Since FCSA-MT is learned *in situ*, there is no retraining required using shifted examples as is necessary with DISN. However, in the comparison between re-trained DISN and FCSA-MT,

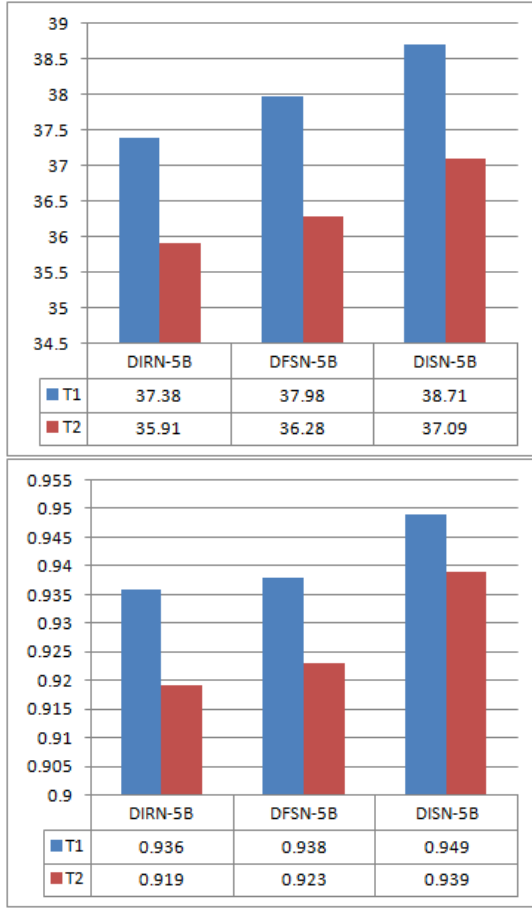


Fig. 14. The PSNR and SSIM of deep multi-contrast CS-MRI inversion algorithms averaged over the test images in the NeoBrainS benchmark.

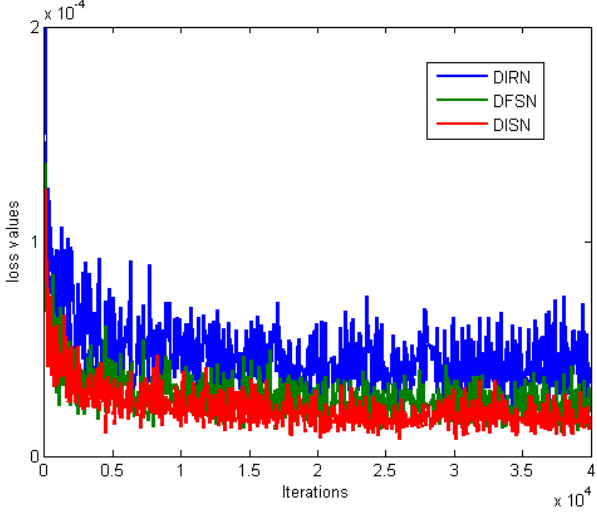


Fig. 15. The training loss function of DIRN-5B, DFSN-5B and DISN-5B.

we observed that DISN is more robust to these pixel shifts. This is shown for the T2 reconstruction as a function of pixel shift in Figure 17.

We observe that FCSA-MT with well-registered MRI pairs outperforms GBRWT, which is the state-of-the-art single-contrast CS-MRI method run only on the shifted T2 data, while the performance of FCSA-MT decreases

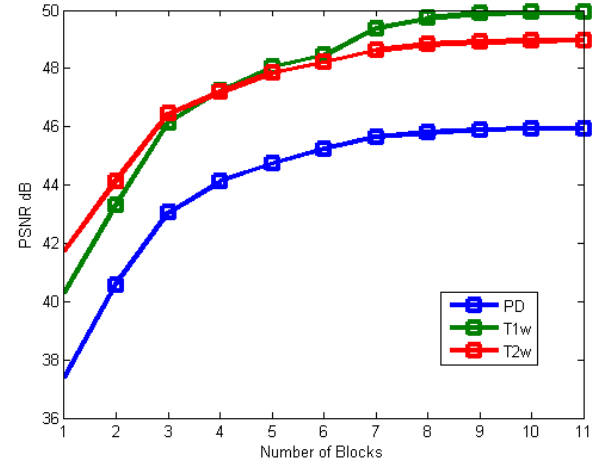


Fig. 16. PSNR curves as a function of the number of blocks.

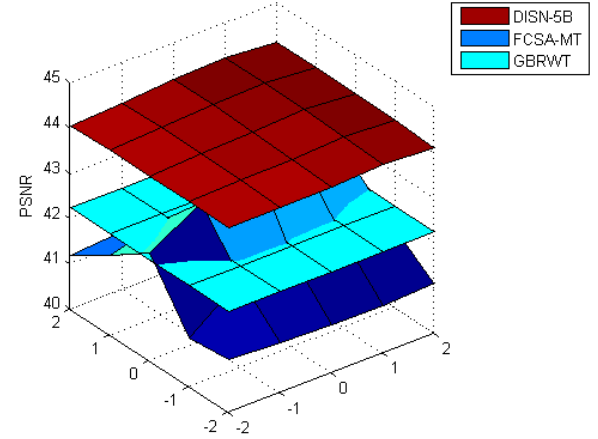


Fig. 17. DISN is robust to non-registration environments compared with conventional single-contrast and multi-contrast MRI. The bottom plane indicates the degree of the pixel shift in each direction, while the vertical axis indicates the respective model performance in PSNR.

dramatically as the shift increases. The DISN model consistently outperforms FCSA-MT and GBRWT regardless of the shift. This helps show that DISN has greater application potential in real-world clinical MRI scenarios.

## VI. CONCLUSION

We have proposed the first deep learning approaches to the multi-contrast CS-MRI inversion problem. The model consists of densely cascaded inference blocks each containing a feature sharing unit and data fidelity unit. The feature sharing strategy can significantly reduce the number of parameters while still obtaining excellent model performance by virtue of the structural similarity across the multiple contrasts. The dense connection between blocks helps to share information across the network in a computationally efficient way. Experiments on three multi-contrast MRI datasets demonstrate that DISN achieves state-of-the-art performance in imaging quality and speed. Furthermore, its robustness to the non-registration environment shows potential for real multi-contrast MRI application.

## REFERENCES

- [1] D. L. Donoho, "Compressed sensing," *IEEE Trans. Inf. Theory*, vol. 52, no. 4, pp. 1289–1306, Apr. 2006.
- [2] E. J. Candès, J. K. Romberg, and T. Tao, "Stable signal recovery from incomplete and inaccurate measurements," *Commun. Pure Appl. Math.*, vol. 59, no. 8, pp. 1207–1223, 2006.
- [3] J. A. Fessler, "Medical image reconstruction: A brief overview of past milestones and future directions," 2017, *arXiv:1707.05927*. [Online]. Available: <https://arxiv.org/abs/1707.05927>
- [4] M. Lustig, D. Donoho, and J. M. Pauly, "Sparse MRI: The application of compressed sensing for rapid MR imaging," *Magn. Reson. Med.*, vol. 58, no. 6, pp. 1182–1195, 2007.
- [5] S. Ma, W. Yin, Y. Zhang, and A. Chakraborty, "An efficient algorithm for compressed MR imaging using total variation and wavelets," in *Proc. Comput. Vis. Pattern Recognit.*, Jun. 2008, pp. 1–8.
- [6] J. Yang, Y. Zhang, and W. Yin, "A fast alternating direction method for TVL1-L2 signal reconstruction from partial Fourier data," *IEEE J. Sel. Topics Signal Process.*, vol. 4, no. 2, pp. 288–297, Apr. 2010.
- [7] J. Huang, S. Zhang, and D. Metaxas, "Efficient MR image reconstruction for compressed MR imaging," *Med. Image Anal.*, vol. 15, no. 5, pp. 670–679, Oct. 2011.
- [8] J. Huang, S. Zhang, and D. Metaxas, "Efficient MR image reconstruction for compressed MR imaging," in *Proc. Int. Conf. Med. Image Comput. Comput.-Assist. Intervent.*, 2010, pp. 135–142.
- [9] X. Qu *et al.*, "Undersampled MRI reconstruction with patch-based directional wavelets," *Magn. Reson. Imag.*, vol. 30, no. 7, pp. 964–977, Sep. 2012.
- [10] X. Qu, Y. Hou, L. Fan, D. Guo, J. Zhong, and Z. Chen, "Magnetic resonance image reconstruction from undersampled measurements using a patch-based nonlocal operator," *Med. Image Anal.*, vol. 18, no. 6, pp. 843–856, 2014.
- [11] Z. Zhan, J.-F. Cai, D. Guo, Y. Liu, Z. Chen, and X. Qu, "Fast multiclass dictionaries learning with geometrical directions in MRI reconstruction," *IEEE Trans. Biomed. Eng.*, vol. 63, no. 9, pp. 1850–1861, Sep. 2016.
- [12] Z. Lai *et al.*, "Image reconstruction of compressed sensing MRI using graph-based redundant wavelet transform," *Med. Image Anal.*, vol. 27, p. 93–104, Jan. 2016.
- [13] S. Ravishankar and Y. Bresler, "MR image reconstruction from highly undersampled k-space data by dictionary learning," *IEEE Trans. Med. Imag.*, vol. 30, no. 5, pp. 1028–1041, May 2011.
- [14] Y. Huang, J. Paisley, Q. Lin, X. Ding, X. Fu, and X.-P. Zhang, "Bayesian nonparametric dictionary learning for compressed sensing MRI," *IEEE Trans. Image Process.*, vol. 23, no. 12, pp. 5007–5019, Dec. 2014.
- [15] S. Wang *et al.*, "Accelerating magnetic resonance imaging via deep learning," in *Proc. IEEE 13th Int. Symp. Biomed. Imag. (ISBI)*, Apr. 2016, pp. 514–517.
- [16] J. Sun, H. Li, and Z. Xu, "Deep ADMM-net for compressive sensing MRI," in *Proc. Adv. Neural Inf. Process. Syst.*, 2016, pp. 10–18.
- [17] G. Yang *et al.*, "DAGAN: Deep de-aliasing generative adversarial networks for fast compressed sensing MRI reconstruction," *IEEE Trans. Med. Imag.*, vol. 37, no. 6, pp. 1310–1321, Dec. 2017.
- [18] T. M. Quan, T. Nguyen-Duc, and W.-K. Jeong, "Compressed sensing MRI reconstruction using a generative adversarial network with a cyclic loss," *IEEE Trans. Med. Imag.*, vol. 37, no. 6, pp. 1488–1497, Jun. 2018.
- [19] D. Lee, J. Yoo, and J. C. Ye, "Deep residual learning for compressed sensing MRI," in *Proc. Int. Symp. Biomed. Imag.*, Apr. 2017, pp. 15–18.
- [20] J. Schlemper, J. Caballero, J. V. Hajnal, A. Price, and D. Rueckert, "A deep cascade of convolutional neural networks for MR image reconstruction," in *Proc. Int. Conf. Inf. Process. Med. Imag.* Springer, 2017, pp. 647–658.
- [21] J. Schlemper, J. Caballero, J. V. Hajnal, A. N. Price, and D. Rueckert, "A deep cascade of convolutional neural networks for dynamic MR image reconstruction," *IEEE Trans. Med. Imag.*, vol. 37, no. 2, pp. 491–503, Oct. 2017.
- [22] Z.-P. Liang and P. C. Lauterbur, *Principles of Magnetic Resonance Imaging: A Signal Processing Perspective*. Bellingham, WA, USA: SPIE Optical Engineering Press, 2000.
- [23] T. Rohlfing, N. M. Zahr, E. V. Sullivan, and A. Pfefferbaum, "The SRI24 multichannel atlas of normal adult human brain structure," *Hum. Brain Mapping*, vol. 31, no. 5, pp. 798–819, 2010.
- [24] G. Huang, Z. Liu, L. van der Maaten, and K. Q. Weinberger, "Densely connected convolutional networks," in *Proc. IEEE Comput. Vis. Pattern Recognit.*, Jul. 2017, pp. 4700–4708.
- [25] A. M. Mendrik *et al.*, "MRBrainS challenge: Online evaluation framework for brain image segmentation in 3T MRI scans," *Comput. Intell. Neurosci.*, vol. 2015, Jan. 2015, Art. no. 1.
- [26] I. Igum *et al.*, "Evaluation of automatic neonatal brain segmentation algorithms: The NeoBrainS12 challenge," *Med. Image Anal.*, vol. 20, no. 1, pp. 135–151, 2015.
- [27] B. Bilgic, V. K. Goyal, and E. Adalsteinsson, "Multi-contrast reconstruction with Bayesian compressed sensing," *Magn. Reson. Med.*, vol. 66, no. 6, pp. 1601–1615, 2011.
- [28] J. Huang, C. Chen, and L. Axel, "Fast multi-contrast MRI reconstruction," in *Proc. Int. Conf. Med. Image Comput. Comput.-Assist. Intervent.* New York, NY, USA: Springer-Verlag, 2012, pp. 281–288.
- [29] S. Ji, Y. Xue, and L. Carin, "Bayesian compressive sensing," *IEEE Trans. Signal Process.*, vol. 56, no. 6, pp. 2346–2356, Jun. 2008.
- [30] S. Cauley, Y. Xi, B. Bilgic, K. Setsompop, J. Xia, and E. Adalsteinsson, "Scalable and accurate variance estimation (SAVE) for joint Bayesian compressed sensing," in *Proc. 21st Annu. Meeting ISMRM*, 2013, p. 2603.
- [31] J. Huang, C. Chen, and L. Axel, "Fast multi-contrast MRI reconstruction," *Magn. Reson. Imag.*, vol. 32, no. 10, pp. 1344–1352, Dec. 2014.
- [32] R. Li, Y. Li, R. Fang, S. Zhang, H. Pan, and J. Huang, "Fast preconditioning for accelerated multi-contrast MRI reconstruction," in *Proc. Int. Conf. Med. Image Comput. Comput.-Assist. Intervent.* Springer, 2015, pp. 700–707.
- [33] J. Yang, J. Wright, T. S. Huang, and Y. Ma, "Image super-resolution via sparse representation," *IEEE Trans. Image Process.*, vol. 19, no. 11, pp. 2861–2873, Nov. 2010.
- [34] J. Yang, J. Wright, T. Huang, and Y. Ma, "Image super-resolution as sparse representation of raw image patches," in *Proc. IEEE Comput. Vis. Pattern Recognit.*, Jun. 2008, pp. 1–8.
- [35] C. Miao and H. Yu, "A general-thresholding solution for  $\ell_p$  ( $0 < p < 1$ ) regularized CT reconstruction," *IEEE Trans. Image Process.*, vol. 24, no. 12, pp. 5455–5468, Dec. 2015.
- [36] A. M. Saxe *et al.*, "On the information bottleneck theory of deep learning," Tech. Rep., 2018.
- [37] N. Tishby and N. Zaslavsky, "Deep learning and the information bottleneck principle," in *Proc. IEEE Inf. Theory Workshop*, Apr./May 2015, pp. 1–5.
- [38] R. Shwartz-Ziv and N. Tishby, "Opening the black box of deep neural networks via information," 2017, *arXiv:1703.00810*. [Online]. Available: <https://arxiv.org/abs/1703.00810>
- [39] S. Bazrafkan, S. Thavalengal, and P. Corcoran, "An end to end deep neural network for iris segmentation in unconstrained scenarios," *Neural Netw.*, vol. 106, pp. 79–95, Oct. 2018.
- [40] Y. Tai, J. Yang, X. Liu, and C. Xu, "MemNet: A persistent memory network for image restoration," in *Proc. Int. Conf. Comput. Vis.*, Oct. 2017, pp. 4539–4547.
- [41] H. Dong, G. Yang, F. Liu, Y. Mo, and Y. Guo, "Automatic brain tumor detection and segmentation using U-Net based fully convolutional networks," in *Proc. Annu. Conf. Med. Image Understand. Anal.* Springer, 2017, pp. 506–517.



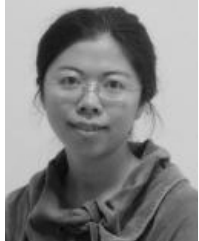
**Liyan Sun** received the B.S. degree from Zhengzhou University, Zhengzhou, China, in 2014. He is currently pursuing the Ph.D. degree with the School of Information Science and Engineering, Xiamen University, Xiamen, China. From 2018 to 2019, he was a Visiting Scholar with the Department of Electrical Engineering, Columbia University, New York, NY, USA. His research interests mainly focus on machine learning, and medical image reconstruction and analysis.



**Zhiwen Fan** received the B.S. degree from Shandong Agriculture University, China, in 2016. He is currently pursuing the master's degree with the Department of Communication Engineering, Xiamen University, China. His research interests mainly focus on image reconstruction and semantic segmentation.



**Xueyang Fu** received the Ph.D. degree in signal and information processing from Xiamen University in 2018. He was a Visiting Student with Columbia University, sponsored by the China Scholarship Council. He is currently an Associate Researcher with the Department of Automation, University of Science and Technology of China. His current research interests include machine learning and image processing.



**Yue Huang** received the B.S. degree from Xiamen University, Xiamen, China, in 2005, and the Ph.D. degree from Tsinghua University, Beijing, China, in 2010. She was a Visiting Scholar with Carnegie Mellon University from 2015 to 2016. She is currently an Associate Professor with the Department of Communication Engineering, School of Information Science and Engineering, Xiamen University. Her main research interests include machine learning and image processing.



**Xinghao Ding** was born in Hefei, China, in 1977. He received the B.S. and Ph.D. degrees from the Department of Precision Instruments, Hefei University of Technology, Hefei, in 1998 and 2003, respectively. He was a Postdoctoral Researcher with the Department of Electrical and Computer Engineering, Duke University, Durham, NC, USA, from 2009 to 2011. Since 2011, he has been a Professor with the School of Information Science and Engineering, Xiamen University, Xiamen, China. His main research interests include machine learning, medical image analysis, and computer vision.



**John Paisley** received the B.S., M.S., and Ph.D. degrees in electrical engineering from Duke University, Durham, NC, USA. He was a Postdoctoral researcher with the Computer Science Departments at University of California at Berkeley, Berkeley, and Princeton University. He is currently an Associate Professor with the Department of Electrical Engineering, Columbia University, New York, NY, USA, where he is also a member of the Data Science Institute. His current research interests include machine learning, focusing on models and inference techniques for text and image processing applications.